

Observation of the Anisotropy of 10 TeV Primary Cosmic Ray Nuclei Flux with the Super-Kamiokande-I Detector

The Super-Kamiokande Collaboration

G. Guillian^{10,*}, J. Hosaka¹, K. Ishihara¹, J. Kameda¹, Y. Koshio¹, A. Minamino¹, C. Mitsuda¹, M. Miura¹, S. Moriyama¹, M. Nakahata¹, T. Namba¹, Y. Obayashi¹, H. Ogawa¹, M. Shiozawa¹, Y. Suzuki¹, A. Takeda¹, Y. Takeuchi¹, S. Yamada¹, I. Higuchi², M. Ishitsuka², T. Kajita², K. Kaneyuki², G. Mitsuka², S. Nakayama², H. Nishino², A. Okada², K. Okumura², C. Saji², Y. Takenaga², S. Desai^{3,†}, E. Kearns³, J.L. Stone³, L.R. Sulak³, W. Wang³, M. Goldhaber⁴, D. Casper⁵, W. Gajewski⁵, J. Griskevich⁵, W.R. Kropp⁵, D.W. Liu⁵, S. Mine⁵, M.B. Smy⁵, H.W. Sobel⁵, M.R. Vagins⁵, K.S. Ganezer⁶, J. Hill⁶, W.E. Keig⁶, K. Scholberg⁷, C.W. Walter⁷, R.W. Ellsworth⁸, S. Tasaka⁹, A. Kibayashi¹⁰, J.G. Learned¹⁰, S. Matsuno¹⁰, M.D. Messier¹¹, Y. Hayato¹², A.K. Ichikawa¹², T. Ishida¹², T. Ishii¹², T. Iwashita¹², T. Kobayashi¹², T. Nakadaira¹², K. Nakamura¹², K. Nitta¹², Y. Oyama¹², Y. Totsuka¹², A.T. Suzuki¹³, M. Hasegawa¹⁴, I. Kato¹⁴, H. Maesaka¹⁴, T. Nakaya¹⁴, K. Nishikawa¹⁴, H. Sato¹⁴, S. Yamamoto¹⁴, M. Yokoyama¹⁴, T.J. Haines¹⁵, S. Dazeley¹⁶, S. Hatakeyama¹⁶, R. Svoboda¹⁶, E. Blaufuss¹⁷, J.A. Goodman¹⁷, G.W. Sullivan¹⁷, D. Turcan¹⁷, A. Habig¹⁸, Y. Fukuda¹⁹, Y. Itow²⁰, M. Sakuda²¹, M. Yoshida²², S.B. Kim²³, J. Yoo²³, H. Okazawa²⁵, T. Ishizuka²⁶, C.K. Jung²⁷, T. Kato²⁷, K. Kobayashi²⁷, M. Malek²⁷, C. Mauger²⁷, C. McGrew²⁷, E. Sharkey²⁷, C. Yanagisawa²⁷, Y. Gando²⁸, T. Hasegawa²⁸, K. Inoue²⁸, J. Shirai²⁸, A. Suzuki²⁸, K. Nishijima²⁹, H. Ishino³⁰, Y. Watanabe³⁰, M. Koshihara³¹, D. Kielczewska^{5,32}, H.G. Berns³³, R. Gran^{33,18}, K.K. Shiraishi³³, A.L. Stachyra³³, K. Washburn³³, R.J. Wilkes³³

and

K. Munakata,²⁴

¹ Kamioka Observatory, Institute for Cosmic Ray Research, University of Tokyo, Hida, Gifu, 506-1205, Japan

² Research Center for Cosmic Neutrinos, Institute for Cosmic Ray Research, University of Tokyo, Kashiwa, Chiba 277-8582, Japan

³ Department of Physics, Boston University, Boston, MA 02215, USA

⁴ Physics Department, Brookhaven National Laboratory, Upton, NY 11973, USA

⁵ Department of Physics and Astronomy, University of California, Irvine, Irvine, CA 92697-4575, USA

⁶ Department of Physics, California State University, Dominguez Hills, Carson, CA 90747, USA

⁷ Department of Physics, Duke University, Durham, NC 27708, USA

⁸ Department of Physics, George Mason University, Fairfax, VA 22030, USA

⁹ Department of Physics, Gifu University, Gifu, Gifu 501-1193, Japan

¹⁰ Department of Physics and Astronomy, University of Hawaii, Honolulu, HI 96822, USA

¹¹ Department of Physics, Indiana University, Bloomington, IN 47405, USA

¹² High Energy Accelerator Research Organization (KEK), Tsukuba, Ibaraki 305-0801, Japan

¹³ Department of Physics, Kobe University, Kobe, Hyogo 657-8501, Japan

¹⁴ Faculty of Science, Kyoto University, Kyoto 606-8502, Japan

¹⁵ Physics Division, P-23, Los Alamos National Laboratory, Los Alamos, NM 87544, USA

¹⁶ Department of Physics and Astronomy, Louisiana State University, Baton Rouge, LA 70803, USA

¹⁷ Department of Physics, University of Maryland, College Park, MD 20742, USA

¹⁸ Department of Physics, University of Minnesota Duluth, MN 55812-2496, USA

¹⁹ Department of Physics, Miyagi University of Education, Sendai, Miyagi 980-0845, Japan

²⁰ Solar-Terrestrial Environment Laboratory, Nagoya University, Nagoya, 464-8601, Japan

²¹ Okayama University, Okayama 700-8530, Japan

²² Department of Physics, Osaka University, Toyonaka, Osaka 560-0043, Japan

²³ Department of Physics, Seoul National University, Seoul 151-742, Korea

²⁴ Shinshu University, Matsumoto 390-8621, Japan

²⁵ International and Cultural Studies, Shizuoka Seika College, Yaizu, Shizuoka 425-8611, Japan

²⁶ Department of Systems Engineering, Shizuoka University, Hamamatsu, Shizuoka 432-8561, Japan

²⁷ Department of Physics and Astronomy, State University of New York, Stony Brook, NY 11794-3800, USA

²⁸ Research Center for Neutrino Science, Tohoku University, Sendai, Miyagi 980-8578, Japan

²⁹ Department of Physics, Tokai University, Hiratsuka, Kanagawa 259-1292, Japan

³⁰ Department of Physics, Tokyo Institute for Technology, Meguro, Tokyo 152-8551, Japan

³¹ The University of Tokyo, Tokyo 113-0033, Japan

³² Institute of Experimental Physics, Warsaw University, 00-681 Warsaw, Poland

³³ Department of Physics, University of Washington, Seattle, WA 98195-1560, USA

(Dated: August 23, 2019)

The relative sidereal variation in the arrival direction of primary cosmic ray nuclei of median energy 10 TeV was measured using downward, through-going muons detected with the Super-Kamiokande-I

detector. The projection of the anisotropy map onto the right ascension axis has a first harmonic amplitude of $(6.64 \pm 0.98 \text{ stat.} \pm 0.55 \text{ syst.}) \times 10^{-4}$ and a phase at maximum at $(33.2^\circ \pm 8.2^\circ \text{ stat.} \pm 5.1^\circ \text{ syst.})$ right ascension. A sky map in equatorial coordinates indicates an excess region in the constellation of Taurus and a deficit region toward Virgo. The excess region is centered at $(\alpha_T, \delta_T) = (75^\circ \pm 7^\circ, -5^\circ \pm 9^\circ)$ with a half opening angle $\chi_T = (39 \pm 7)^\circ$; the excess flux is $(0.104 \pm 0.020)\%$ above the isotropic expectation. The corresponding parameters for the deficit region are $(\alpha_V, \delta_V) = (205^\circ \pm 7^\circ, 5^\circ \pm 10^\circ)$, $\chi_V = (54 \pm 7)^\circ$, and $(-0.094 \pm 0.014)\%$. The data do not allow us to rule out a pure dipole form for the anisotropy (allowed at 13% confidence level); they are better described by the excess and deficit cones described above. We explored the implications under the assumption that the true anisotropy is not distorted too much by the analysis filter so that it is well-described by the observed excess and deficit cones.

PACS numbers: 95.85.Ry, 96.50.Bh

I. INTRODUCTION

The flux of cosmic rays with energy per nucleon in the range $10^{11} \sim 10^{14}$ eV is known to have a sidereal anisotropy of several times 10^{-4} . The anisotropy is due to a combination of effects. Compton and Getting [1] proposed in 1935 that the motion of the solar system relative to the rest frame of the cosmic ray plasma should cause an energy-independent dipole anisotropy whose maximum is in the direction of this motion. Solar diurnal and seasonal changes in the atmospheric temperature can induce a sidereal variation in the cosmic ray rate [2]. The anisotropy that remains after accounting for these effects is presumably of Galactic origin, with possible modulations due to the heliosphere (see, for example, [3, 4]) and, at the lowest energies, solar wind and magnetic field.

In this article, we present a report on the observation of cosmic ray anisotropy with the Super-Kamiokande I (SK-I) detector. SK-I can make a unique contribution to this subject because of the large overburden and detector size. The overburden makes SK-I sensitive to primary cosmic ray energies normally attainable with extensive air shower arrays, while the large statistics and excellent muon tracking resolution enabled the creation of a two dimensional map of the anisotropy, which is the first-published muon-based map [5].

II. THE DETECTOR AND THE DATA

SK-I is a 50 kiloton underground imaging water Cherenkov detector in Kamioka, Japan at geographical coordinates $36^\circ 25' 32.6''$ N, $137^\circ 18' 37.1''$ E and an altitude of 370 m above sea level. The vertical overburden is about 1000 meters, or 2700 meters water equivalent. The detector's design was optimized for the detection of neutrinos and nucleon decay; the placing of the detector under large overburden to shield against cosmic ray

muons is an important part of this design. The overburden shields all charged cosmic ray secondaries except muons with energy above 0.8 TeV. The portion of the detector sensitive to muons is a cylinder of diameter 33.8 m and height 36.2 m, giving a target area between 1000 m² and 1200 m² depending on the zenith angle. The average cosmic ray muon event rate was 1.8 Hz. More details about the SK-I detector are reported in [6].

The data used in this analysis were collected between June 1, 1996 and May 31, 2001. During this period, the detector was live for 1662.0 days (91.0% of the time) and registered 2.54×10^8 muon events. Muon track reconstruction was performed with an algorithm developed in SK-I to examine the spatial correlation between spallation products and parent muons in the solar neutrino analysis [7]. In order to maintain the angular resolution within 2° , the muon tracks were required to be longer than 10 m and downward-going; 82.6% of the events (2.10×10^8) satisfied these requirements. The reliability of using muon tracks for astronomical purposes was confirmed by the observation of the shadow of the moon and the sun [8].

The relationship between the energy of the detected muon and the energy of the primary cosmic ray that produced it is described by a response function (see, for example, Ref. [9]). For SK-I, the threshold muon energy is 0.8 TeV for the thinnest part of the overburden. The corresponding median primary cosmic ray energy is about ten times larger [9], while the spread in the primary cosmic ray energy is about an order of magnitude above and below the median. SK-I is, therefore, sensitive to primary cosmic rays with energy in the range several TeV to several hundred TeV.

The variation in the overburden along different lines of sight explains most of the features seen in the muon event rate in the horizontal coordinate system (Fig. 1). This variation implies that the muon threshold energy, and, therefore, the median primary cosmic ray energy, vary with direction. A given point in the celestial coordinate system traces out a trajectory of fixed declination as the Earth rotates; the overburden along the line of sight to this point varies with this motion. For instance, the thickness of the overburden at the apex of the declination = 0° trajectory is about 2300 meters water equivalent, which corresponds to a median primary cosmic

*Present address: Physics Department, Queen's University, Kingston, Ontario, Canada K7L 3N6

†Present address: Center for Gravitational Wave Physics, Pennsylvania State University, University Park, PA 16802 USA

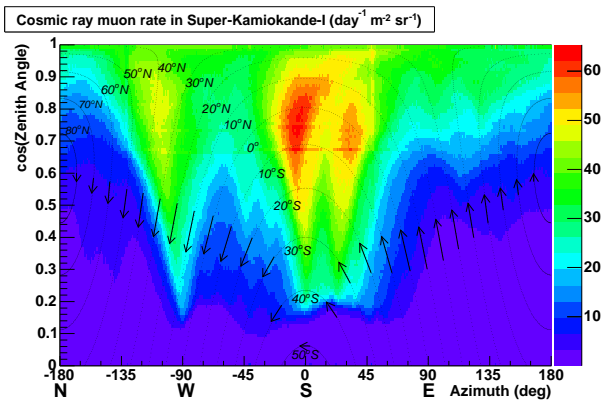


FIG. 1: Event rate ($\text{day}^{-1}\text{m}^{-2}\text{sr}^{-1}$) in horizontal coordinates. The dotted curves indicate contours of constant declination, while the arrows indicate the apparent motion of stars with the rotation of the earth.

ray energy of about 8 TeV. In contrast, the corresponding thickness and median energy for declination = 50° S are 3800 meters water equivalent and 20 TeV, respectively. The average overburden over one rotation period is, therefore, a function of declination, which implies that the primary cosmic ray spectrum seen by SK varies with declination. For this reason, the anisotropy presented here is a spectrum-weighted average over a broad range of energies spanning several to several hundred TeV.

It is seen from Fig. 1 that the detector is most sensitive to cosmic rays originating from the south. During 5 years' operation of SK-I, the most sensitive direction was exposed to every 1° RA slice of the celestial sphere for an average of about 4.6 days. The exposure, however, was unequal for different directions because the detector was dead for several minutes almost every day, with occasional periods of down time lasting many hours. Periods of detector down time were not random, but occurred more often during day time hours. These periods of dead time, accumulated over five years, introduce fluctuations in the exposure times for different directions. The maximum and minimum deviations from the average exposure were $+1.4\%$ and -1.3% . In the celestial coordinate analysis of Sec. III, the rates were corrected to account for different measured detector live time in different sidereal time bins.

The atmosphere is a part of the detector in the sense that it is responsible for converting primary cosmic rays into muons that can penetrate the overburden. It is a dynamic detector component because its density changes with temperature and pressure, and the muon rate changes accordingly. The relative variation in the muon rate due to atmospheric variation has relatively strong Fourier components with frequencies corresponding to one year and one solar day. The solar diurnal component of the muon rate is, to some extent, modulated by a seasonally varying signal, giving rise to spurious sidereal variation. The magnitude of this variation is large (comparable to the true magnitude) when the observation period is restricted seasonally. However, averaged

over exact-year periods, the spurious variation largely cancels out; we estimate it to be only 18% of the true magnitude. For this reason, we chose our data to span the exact five year period between June 1, 1996 and June 1, 2001. In the celestial coordinate analysis below, we statistically subtract this spurious variation from the observed signal using the method of Farley and Storey [2]. This subtraction introduces an uncertainty of about 10% to the true magnitude of the sidereal anisotropy [35]. Technical details on the subtraction of the spurious atmospheric effect is given in Appendix A. It is also important to verify that the input to this correction is sound; we show in Appendix B that the monthly muon rate variation, which is primarily due to atmospheric effects, is properly measured in Super-Kamiokande.

Another correction that can be made to the anisotropy measurement is that for the Compton-Getting effect. We chose not to subtract this in our main result because the rest frame of the cosmic ray plasma – an important input for the subtraction – is not known. In principle this can be measured with our data by measuring the seasonal change in the anisotropy. When the earth's orbital phase is such that the orbital velocity moves against the bulk cosmic ray motion, the flux is enhanced in this direction; six months later, the effect should be smaller, as the earth moves along with the bulk motion and the relative velocity between the observer and the cosmic ray rest frame is at a minimum. In practice, however, the cosmic ray rest frame was not measurable in this manner because the seasonal change in the flux introduced by atmospheric effects was much larger than the Compton-Getting signal. In the literature, two cosmic ray rest frames are often assumed: (1) the local standard of rest (the frame of the average motion of stars in the neighborhood of the sun); (2) the rest frame of the local interstellar medium. Appendix C gives the result of anisotropy measurements with the subtraction of the Compton-Getting effect assuming these two rest frames, and the resulting anisotropy parameters are summarized in tables IV and V.

III. CELESTIAL COORDINATE ANALYSIS

In this section, we describe the celestial coordinate analysis of the anisotropy. First, the general mathematical framework of the analysis is given. An important part of this discussion is the distortion introduced to the anisotropy map by the analysis method. In the second subsection, the implementation of the method to the data is described. In the third subsection, the anisotropy in one dimension (i.e. as a function of right ascension) is presented. This is followed by the anisotropy map in two dimensions.

A. Analysis Method: Mathematical Framework and the Distortion Introduced to the Anisotropy Map

The number of downward-going muon events from the celestial coordinates (α, δ) observed in SK-I may be expressed as follows:

$$N(\alpha_i, \delta_j) = \sum_k^{N_{sid}} [1 + \epsilon(\alpha_i, \delta_j)] \cdot R(\alpha_i - \tau_k, \delta_j) \cdot T_k \cdot d\Omega_{i,j} \quad (1)$$

The indexes i, j , and k are for the right ascension, declination, and sidereal time, N_{sid} is the number of sidereal time bins, and T_k is the total detector live time in the sidereal time bin k . The function $R(\alpha - \tau, \delta)$ is the differential event rate for an isotropic cosmic ray flux in the detector coordinate system (parameterized by hour angle and declination). The form of this function is determined by the overburden and the zenith angle dependence of the cosmic ray flux. The function $\epsilon(\alpha, \delta)$ represents the true cosmic ray anisotropy.

As stated in the previous section, the term T_j in Eqn. 1 varies by $\begin{smallmatrix} +1.4\% \\ -1.3\% \end{smallmatrix}$. This variation of purely instrumental origin was removed by multiplying each sidereal time bin by the following weight:

$$w_k = \frac{\langle T \rangle}{T_k} \quad (2)$$

Once this correction is made, the raw anisotropy data can be expressed as follows:

$$\begin{aligned} n(\alpha_i, \delta_j) &= \sum_k^{N_{sid}} [1 + \epsilon(\alpha_i, \delta_j)] \cdot R(\alpha_i - \tau_k, \delta_j) \quad (3) \\ &= [1 + \epsilon(\alpha_i, \delta_j)] \cdot \rho(\delta_j) \end{aligned}$$

In the second line, $\rho(\delta_j) = \sum_k^{N_{sid}} R(\alpha_i - \tau_k, \delta_j)$ - i.e. the summation of hour angle erases the right ascension dependence because of the cyclical nature of the function R . In other words, the sum is independent of the starting point, specified by α_i .

Ideally, one would like to extract the anisotropy function $\epsilon(\alpha, \delta)$ from the data. In practice, this cannot be done because the declination dependence for an isotropic flux, $\rho(\delta)$, can neither be measured from the data nor calculated to an accuracy required to extract an anisotropy of order several parts per 10,000. However, $\rho(\delta)$ can be factored out by calculating the following ratio:

$$\begin{aligned} A(\alpha_i, \delta_j) &= \frac{n(\alpha_i, \delta_j) - \langle n(\delta_j) \rangle}{\langle n(\delta_j) \rangle} \quad (4) \\ &\approx \epsilon(\alpha_i, \delta_j) - \langle \epsilon(\delta_j) \rangle \quad (5) \end{aligned}$$

The second line is an approximation that ignores second and higher order terms in ϵ . The averages indicated by the brackets is over right ascension bins. Explicitly,

$$\begin{aligned} \langle n(\delta_j) \rangle &= \frac{1}{N_\alpha} \cdot \sum_i^{N_\alpha} n(\alpha_i, \delta_j) \quad (6) \\ &= [1 + \langle \epsilon(\delta_j) \rangle] \cdot \rho(\delta_j) \end{aligned}$$

$$\langle \epsilon(\delta_j) \rangle = \frac{1}{N_\alpha} \sum_i^{N_\alpha} \epsilon(\alpha_i, \delta_j) \quad (7)$$

The second term in Eqn. 5 distorts the true anisotropy function $\epsilon(\alpha, \delta)$ in an unknown, but restricted way. As an illustration of the nature of the distortion, let us imagine that, for a fixed declination δ , $\epsilon(\alpha, \delta)$ is well-described by a sinusoidal function; this function can be written as a sum of a constant offset $\langle \epsilon(\delta) \rangle$ and a sinusoidal term whose average is zero. The second term in Eqn. 5 removes the constant offset. In more precise mathematical terms, this distortion can be described as follows. The spherical harmonic decomposition of $\epsilon(\alpha, \delta)$ is:

$$\epsilon(\alpha, \delta) = \sum_{\ell, m} a_{\ell, m} \cdot Y_{\ell, m}(\alpha, \lambda) \quad (8)$$

The angle $\lambda = \pi/2 - \delta$ is the complement of the declination, and it is measured relative to the z axis (Earth's rotation axis) in the usual notation for spherical harmonics. The modified anisotropy function $A(\alpha, \delta)$ is related to this as follows:

$$\begin{aligned} A(\alpha, \delta) &= \sum_{\ell, m} a_{\ell, m} \cdot \left[Y_{\ell, m}(\alpha, \lambda) - \frac{1}{2\pi} \int d\alpha' Y_{\ell, m}(\alpha', \lambda) \right] \\ &= \sum_{\ell, m} b_{\ell, m} \cdot Y_{\ell, m}(\alpha, \lambda) \quad (9) \end{aligned}$$

The new coefficients $b_{\ell, m}$ have the following values:

$$b_{\ell, m} = \begin{cases} 0 & m = 0 \\ a_{\ell, m} & m \neq 0 \end{cases} \quad (10)$$

It is seen that the axisymmetric terms (i.e. $m = 0$ terms) are zeroed out.

As a concrete example, consider the effect of the distortion on the first harmonic of an axisymmetric anisotropy (i.e. a dipole anisotropy) of magnitude D along an arbitrary direction (α_0, δ_0) in equatorial coordinates. The anisotropy function has the following form:

$$A(\alpha, \delta) = D [\cos \delta \cos \delta_0 \cos(\alpha - \alpha_0) + \sin \delta \sin \delta_0] \quad (11)$$

After subtracting the constant offset, this becomes:

$$\tilde{A}(\alpha, \delta) = D \cos \delta_0 \cos \delta \cos(\alpha - \alpha_0) \quad (12)$$

$$= \tilde{D} \cos \delta \cos(\alpha - \alpha_0) \quad (13)$$

The second line is the form of the anisotropy for the projection of the original dipole in the equatorial plane; the dipole strength $\bar{D} = D \cos \delta_0$ is the length of this projection.

Functions with higher harmonics behave in more complicated ways. For instance, consider an anisotropy function that can be described with two cones, one with excess flux, the other with a deficit flux. If these two cones are not 180° opposite one another, significant contributions from higher harmonics must, by necessity, be present. If the declination of the two cones is similar, then the distortion is small (the excess cone cancels out the deficit cone, making the constant offset small). If they are different, the distortion pushes the declination of the two cones towards each other, while the right ascension is not affected at all.

B. Analysis Method: Implementation

In the analysis presented here, the cosmic ray anisotropy in the celestial sphere was plotted in one and two dimensions. The two dimensional map corresponds to $A(\alpha, \delta)$ shown in Eqn. 4. The one dimensional map can be plotted either as a function of right ascension or sidereal time. In the former, the plot corresponds to the following:

$$a(\alpha_i) = \frac{m(\alpha_i) - \langle m \rangle}{\langle m \rangle}, \quad (14)$$

where $m(\alpha)$ is defined as:

$$m(\alpha_i) = \sum_j^{N_\delta} n(\alpha_i, \delta_j), \quad (15)$$

$\langle m \rangle$ corresponds to $m(\alpha)$ averaged over right ascension, and the function $n(\alpha, \delta)$ is defined in Eqn. 3. The one dimensional map as a function of sidereal time is defined as follows:

$$\tilde{a}(\tau_k) = \frac{\tilde{m}(\tau_k) - \langle \tilde{m} \rangle}{\langle \tilde{m} \rangle} \quad (16)$$

The function $\tilde{m}(\tau_k)$ is defined as:

$$\tilde{m}(\tau_k) = \sum_i^{N_\alpha} \sum_j^{N_\delta} [1 + \epsilon(\alpha_i, \delta_j)] \cdot R(\alpha_i - \tau_k, \delta_j), \quad (17)$$

and $\langle \tilde{m} \rangle$ is the average of $m(\tau)$ over sidereal time.

In practice, the one dimensional anisotropy plot $a(\alpha)$ is made by first making a histogram of the muon track right ascension, where each entry is weighted by w_k in Eqn. 2 in order to equalize the exposure to all directions in the celestial sphere (the value of the weight is $1 \pm \epsilon$,

with the correction ϵ about 1%). The relative variation of this histogram about its mean corresponds to $a(\alpha)$. The two dimensional anisotropy $A(\alpha, \delta)$ is made exactly like $a(\alpha)$, but in 10° strips of declination. Finally, the one dimensional plot $\tilde{a}(\tau)$ is made by making a histogram of the number of muon events in sidereal time bins, dividing this bin-by-bin with a histogram of the detector live time in sidereal time bins, and taking the variation relative to the mean. The function $\tilde{a}(\tau)$ can also be thought of as $a(\alpha)$ with α replaced with τ . The shape of the resulting function is similar to that of $a(\alpha)$ because $R(\alpha - \tau, \delta)$ is generally largest when $\alpha \approx \tau$ (Fig. 1). In other words, at any given moment, the right ascension of a muon track measured with SK is approximately equal to the sidereal time, or to the right ascension of the zenith. For this reason, we shall refer to $\tilde{a}(\tau)$ as the ‘zenith-type’ anisotropy, while $a(\alpha)$ shall be referred to as the ‘track-type’ anisotropy because it is made using information from muon tracks. The ‘zenith-type’ anisotropy is equivalent to smearing the ‘track-type’ anisotropy. Clearly, the function $a(\alpha)$ is a better probe of cosmic ray anisotropy than $\tilde{a}(\tau)$, but we have, nevertheless, produced $\tilde{a}(\tau)$ because most other underground muon measurements are presented in this way.

Spurious sidereal variation of atmospheric origin described in Sec. II was subtracted from all plots and maps unless otherwise noted. The spurious variation has little effect on the best fit value of the parameters describing the anisotropy, but it significantly increases the uncertainty.

C. Right Ascension Distribution

A track-type plot of the right ascension of cosmic rays before subtracting the spurious sidereal anisotropy from atmospheric effects is shown as data points in Fig. 2 (a). The solid curve is the best fit of the first two harmonics to the data, while the dashed curve (almost overlapping the solid one) is the sidereal variation after correcting for the atmospheric effect. The curves are parameterized as follows:

$$F(x) = A_1 \cdot \cos \left[\frac{\pi}{180} \cdot (x - \phi_1) \right] + A_2 \cdot \cos \left[\frac{2\pi}{180} \cdot (x - \phi_2) \right] \quad (18)$$

The best fit parameters are summarized in Table I. The parameter errors are statistical, except measurements with atmospheric correction (TRACK/CORR. and ZENITH/CORR.), where the first error is statistical and the second error is the systematic error introduced by subtraction of the atmospheric effect (see Appendix A).

The zenith-type plot of cosmic ray right ascension is shown in Fig. 2 (b). The fit parameters of (b) are similar to those of (a), but the amplitudes are smaller, which is consistent with the fact that (b) is obtained by smearing (a).

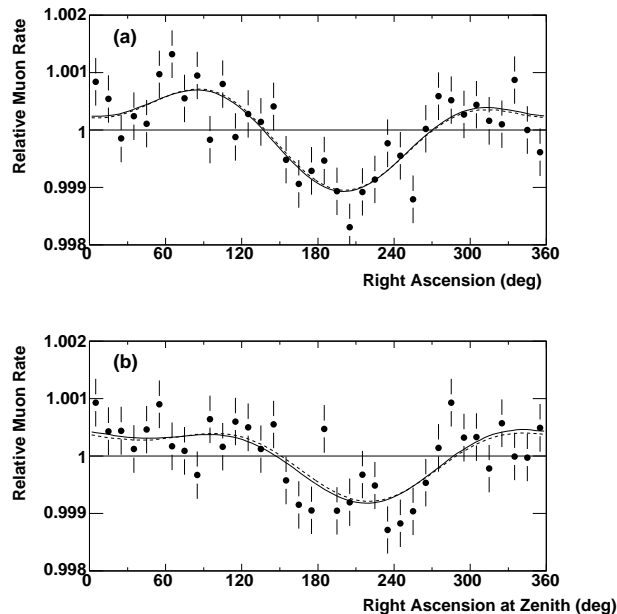


FIG. 2: (a) Track-type right ascension projection plot. (b) Zenith-type plot. The error bars represent statistical errors. The solid curve in each frame is the best fit of the first two harmonic functions. The dashed curve (almost overlapping the solid curve) is the first two harmonics after subtracting the atmospheric contribution.

Anisotropy measurements based on zenith-type plots from Kamiokande [10] and MACRO [11] (both deep underground experiments like SK-I) are also summarized in Table I. Only the first term in Eqn. 18 was fit to their data. The amplitude and phase show good agreement with those of SK-I.

Figure 3 shows the amplitude and phase of the best-fit first harmonic function fit to zenith-type plots from numerous experiments. The SK-I result is consistent with the trend.

D. Sky Map of the Anisotropy

An anisotropy map in the celestial sphere is obtained by making track-type plots in 10° strips of declination, giving $10^\circ \times 10^\circ$ pixels. The result is shown in Fig. 4 (smoothing applied for visual purposes only). Each $10^\circ \times 10^\circ$ cell in map (a) shows the fractional variation from the isotropic case, while that in (b) shows the standard deviation of this variation. The fractional variations from isotropy are large and erratic in (a) because of oversampling, but the positive and negative variations are clearly clustered. In order to optimize the binning, as well as to identify and characterize the excess and deficit regions, we used a clustering algorithm described in Appendix D. The algorithm indicates a unique region of excess in the direction of the constellation Taurus (α_T, δ_T)

$= (75^\circ \pm 7^\circ, -5^\circ \pm 9^\circ)$, while a unique region of deficit was found in the constellation of Virgo (α_V, δ_V) = $(205^\circ \pm 7^\circ, 5^\circ \pm 10^\circ)$. The half opening angle of the “Taurus” region is $39^\circ \pm 7^\circ$ with a relative rate $(0.104 \pm 0.020)\%$ above average, while the size of the “Virgo” region is $54^\circ \pm 7^\circ$ with a relative rate of $(0.094 \pm 0.014)\%$ below average. All errors are statistical (see Appendix D for the method used to obtain the statistical error of reconstructed cone parameters). These results are summarized in Table II.

The observed anisotropy is unlikely to be due to a random fluctuation of an isotropic cosmic ray flux. The calculation of the statistical significance and the rejection of the null hypothesis are performed as follows. The number of events in the Taurus excess cone is $(0.104 \pm 0.020)\%$ above the expectation from the isotropic distribution, which corresponds to a gaussian probability of 2.0×10^{-7} . However, since the entire sky above the horizon was searched with a variable half-opening angle, the actual probability for this sort of deviation to occur is larger by some trials factor. In order to determine this, 1×10^7 isotropic sky maps were generated with statistical fluctuations generated with a random number generator. To cover the angular size of the Taurus excess, we counted the number of maps with reconstructed cone with in-cone standard deviation > 5.2 sigma and half-opening angle between 30° and 60° . The number of such maps was 378 out of 10^7 generated maps, giving a post-trials probability of 3.78×10^{-5} . Similarly, the number of events in the Virgo deficit cone is $(0.094 \pm 0.014)\%$ below the isotropic expectation, which is a 6.7 standard deviation effect corresponding to a gaussian probability of 2.1×10^{-11} . Among the 1×10^7 generated maps, none had a deviation as large as observed with half-angle between 30° and 60° . We, therefore, set a 90% confidence level upper limit of the post-trials probability at 2.3×10^{-7} .

Finally, we note that comparison of the averages between different declination bands are not meaningful; the above analysis is, therefore, insensitive to the excess/deficit from the direction of the celestial poles. In other words, the 2-dimensional anisotropy can be thought of as a series of 1-dimensional curves in consecutive strips of declination. Before going through the analysis filter, each curve is described by a constant offset corresponding to the average flux, and a sum of harmonics whose average is zero. The filter removes the constant offset, keeping all other terms intact. Thus, the analysis presented here is insensitive to any anisotropy along Earth’s rotation axis.

IV. THE ROBUSTNESS OF THE OBSERVED ANISOTROPY

The result of the analysis is insensitive to the exact choice of the track length and zenith angle cuts. As an illustration of this insensitivity, track-type plots were made for 60 combinations of track length and zenith angle cuts; the former was varied between 0 and 20 m, and the latter

1	2	3	4	5	6	7	8	9	10	11	
EXP	PLOT TYPE	AREA (m ²)	DEPTH (m.w.e.)	LT (days)	EVENTS ($\times 10^6$)	A_1 ($\times 10^{-4}$)	ϕ_1 (DEG)	A_2 ($\times 10^{-4}$)	ϕ_2 (DEG)	χ^2/dof	
SK-I	TRACK/CORR.	≈ 1000	~ 2700	1662	210	$6.6 \pm 1.0 \pm 0.6$	$33 \pm 8 \pm 5$	4.1 ± 1.0	106 ± 7	—	
	TRACK/UNC.					6.8 ± 1.0	30 ± 8				35.1/32
	ZENITH/CORR.					$5.3 \pm 1.0 \pm 0.7$	$40 \pm 10 \pm 10$				—
	ZENITH/UNC.					5.7 ± 1.0	35 ± 10				38.5/32
KAM	ZENITH	≈ 150		2072	59	5.6 ± 1.9	8 ± 19	—	—	0.3/6	
MAC	ZENITH	≈ 1000	~ 3800	2145	44	8.2 ± 2.7	-12 ± 20	—	—	4.6/5	

TABLE I: Summary of one dimensional anisotropy measurements from deep underground muon telescopes. Col. 1: SK-I, KAM, and MAC refer to the SK-I, Kamiokande [10], and MACRO [11] experiments. Col. 2: type of plot. TRACK = track-type plot, ZENITH = zenith-type. CORR. = plot corrected for spurious sidereal anisotropy of atmospheric origin, UNC. = plot uncorrected for this. Col. 3: nominal value of detector projected area, in m². Col. 4: nominal value of the overburden, in m.w.e.. Col. 5: total detector live time, in days. Col. 6: total number (millions) of events. Cols. 7-10: Best fit first and second harmonic amplitude and phase. Errors are statistical except entries with two errors, where the first error is statistical and the second is the systematic error introduced in subtracting the atmospheric effect. Col. 11: χ^2 per degree of freedom of fit of Eqn. 18 to the data (χ^2 does not apply to data corrected for the atmospheric effect). The second harmonic amplitude and phase are the same for the corrected and uncorrected result because the spurious atmospheric anisotropy is assumed to vary as a first harmonic function. Kamiokande and MACRO report only a first harmonic fit to their data.

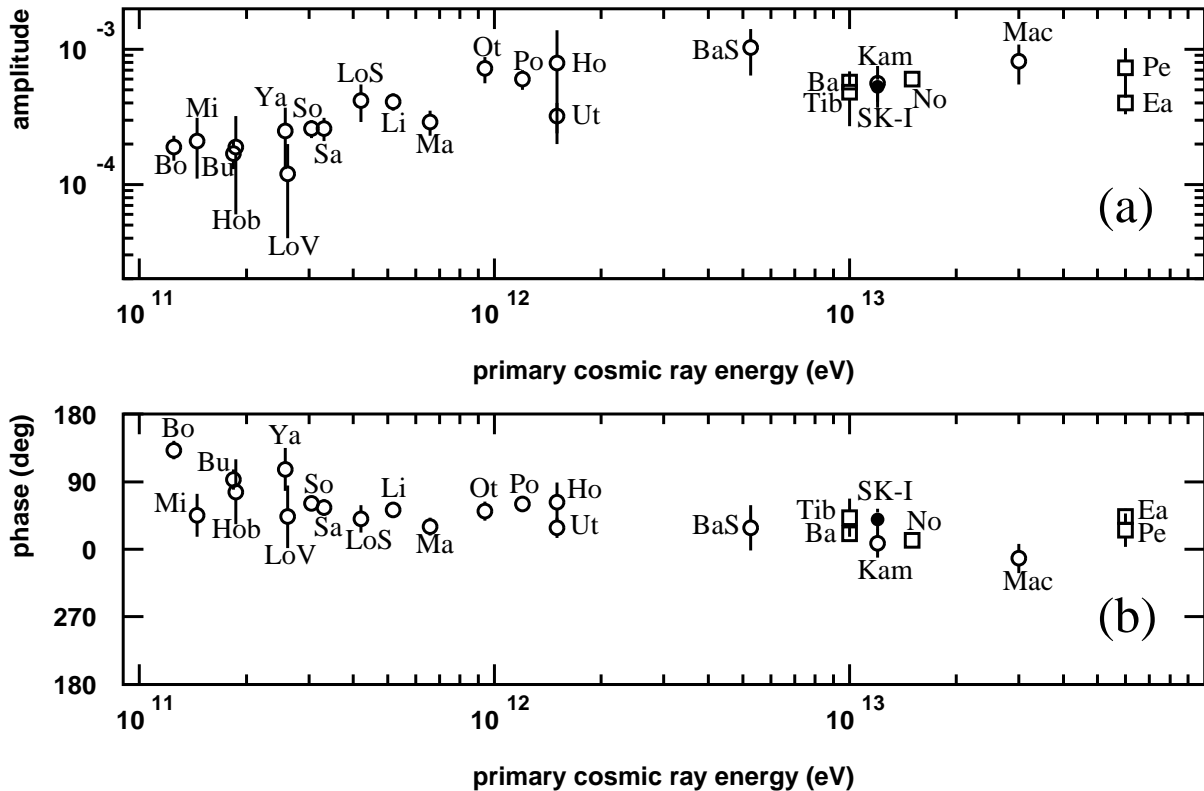


FIG. 3: Amplitude and phase of the first harmonic fit to zenith-type plots from various cosmic ray experiments. The energy in the horizontal axis is either the median or the log-mean energy. Circles: muon detectors. Squares: extensive air shower array. Filled circle: SK-I. Data references: Bo = Bolivia (vertical) [12], Mi = Misato (vertical) [13], Bu = Budapest [13], Hob = Hobart (vertical) [13], Ya = Yakutsk [13], LoV = London (vertical) [13], So = Socomo (vertical) [12], Sa = Sakashita (vertical) [14], LoS = London (south) [15], Li = Liapootah (vertical) [16], Ma = Matsushiro (vertical) [17], Ot = Ottawa (south): [18], Po = Poatina (vertical) [19], Ho = Hong Kong [20], Ut = Utah [21], BaS = Baksan (south) [22], SK-I (this report), Kam = Kamiokande [10], Mac = MACRO [11], Tib = Tibet (vertical) [23], Ba = Baksan air shower [24], No = Mt. Norikura [3], Ea = EAS-TOP [25], Pe = Peak Musala [26].

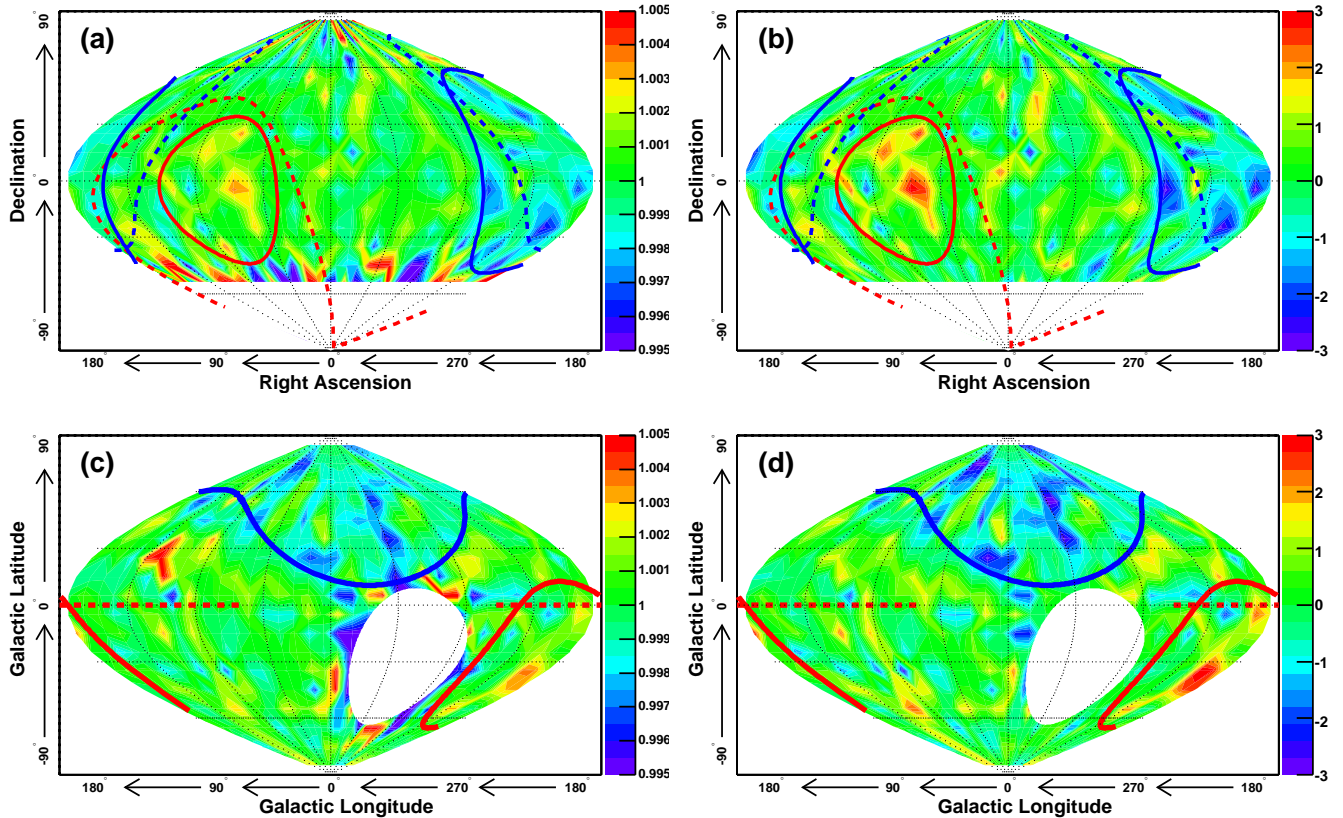


FIG. 4: Sky map of the anisotropy in equatorial coordinates. The sky is divided into $10^\circ \times 10^\circ$ cells (Gouraud smoothing applied only for visual purposes). Declinations less than -53.58° (white region) always lie below the horizon and are thus invisible to the detector. In (a), each cell shows the fractional variation from the isotropic flux, while in (b) it shows the standard deviation of this variation. The solid red and blue curves show the excess and deficit cones obtained using a clustering algorithm applied to the data. The dashed curves in (a,b) show excess and deficit cones from the NFJ model [4], which is described in Section V. (c) and (d) show the maps in (a) and (b) transformed to the galactic coordinates. The solid red and blue curves are the same cones as described above. The dashed red horizontal line indicates the direction of the Orion arm. The white patch indicates the below-horizon region.

1	2	3	4	5	6
REGION TYPE	NAME	CONE SOURCE	(α, δ)	SIZE	DEVIATION
EXCESS	TAURUS	OBSERVED, CORR.	$(75^\circ, -5^\circ)$	39°	$(0.104 \pm 0.020)\%$
		OBSERVED, UNC.	$(65^\circ, 5^\circ)$	27°	$(0.140 \pm 0.026)\%$
	TAIL-IN	NFJ MODEL	$(90^\circ, -24^\circ)$	68°	—
DEFICIT	VIRGO	OBSERVED, CORR.	$(205^\circ, 5^\circ)$	54°	$(-0.094 \pm 0.014)\%$
		OBSERVED, UNC.	$(205^\circ, 5^\circ)$	54°	$(-0.099 \pm 0.014)\%$
	GALACTIC	NFJ MODEL	$(180^\circ, 20^\circ)$	57°	—

TABLE II: Cone parameters of excess and deficit regions. The NFJ model is described in Section V. Column 3 describes whether the cone is from observation or model, and whether or not the atmospheric correction has been applied. Columns 4 and 5 show the center and half opening angle of the cones. Column 6 shows the deviation from the isotropic event rate in the contained regions (the error is the statistical error based on the number of events contained in the cone). Rows labeled “CORR.” and “UNC.” refer, respectively, to cones obtained from the anisotropy map corrected and uncorrected for atmospheric effects.

between 30° above horizontal to 90° below horizontal (i.e. no zenith angle cut). The harmonic function Eqn. 18 was fit to each plot, and the RMS spread for each of the four parameters was found to be within 50% of the statistical error.

As a test of signal robustness, the data were divided into five exact-year periods spanning June 1st to May 31st of every year from 1996 to 2000, and a measurement of anisotropy from the track-type plot was made on each set. The best fit first harmonic amplitude and phase are

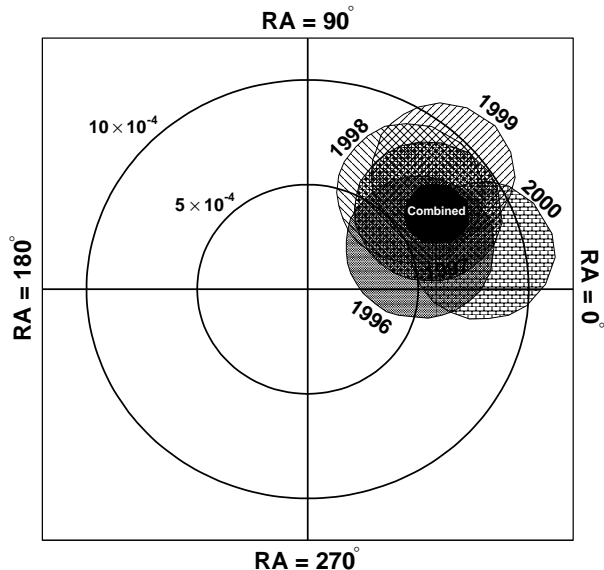


FIG. 5: The 2-parameter 68% confidence level regions ($\Delta\chi^2 = 2.3$) of the amplitude and phase of the first harmonic function fit to yearly track-type anisotropy plots. The radial distance from the origin is the first harmonic amplitude, while the counterclockwise angle from $RA = 0^\circ$ is the right ascension at maximum. The regions are labeled by the corresponding year. The label “Combined” indicates the contour from the 5-year combined data set.

shown in Fig. 5, together with their 2-parameter 68% confidence level regions. Good overlap is seen. The fact that the phase is consistent from year to year is strong evidence that the observed anisotropy is due to a real physical effect.

V. DISCUSSION

The near-isotropy of cosmic rays with energy per nucleus below the “knee” in the spectrum is usually described as follows. At these energies, strong evidence exists to indicate that primary cosmic ray nuclei mostly originate as interstellar matter in the Milky Way Galaxy. They are accelerated by blast waves from supernova remnants, and are effectively trapped in the Milky Way by the Galactic magnetic field with a strength of order several micro-Gauss. The gyro-radius of a 10^{11} eV $\sim 10^{14}$ eV proton propagating in a uniform micro-Gauss level magnetic field is in the range ~ 10 AU and ~ 0.1 pc, much smaller than the thickness of the Galactic disk of $200 \sim 300$ pc. The motion of cosmic ray nuclei is spiral-like in regions of the Galaxy where the magnetic field is smooth. Interspersed in these regions are areas where the magnetic field is irregular, in which the trajectories are complex and the direction before and after entrance in these areas is nearly random. Over large distance scales,

the irregular regions can be thought of as scatterers of cosmic rays. As a result, the average motion of cosmic rays in the Galaxy is expected to be highly random, which is consistent with the observed near-isotropy of the flux.

The anisotropy at these energies is presumably due to a number of mechanisms. At the largest scales, the distribution of cosmic ray sources, the large-scale configuration of the Galactic magnetic field, the distribution of magnetic field irregularities, and the location of the solar system in the Galaxy are all expected to be contributing factors. At smaller scales, the magnetic field configuration in the neighborhood of the solar system and the distribution of the nearest cosmic ray sources should contribute. At the smallest scales, the solar magnetic field can be ruled out at these energies, although there are suggestions that the heliosphere may play a role at energies around ~ 1 TeV (e.g. [4]). Of course, the Compton-Getting effect is expected to produce a dipole anisotropy on top of all of the above. The relative importance of each of these effects is not known.

As stated in section III, Earth-based cosmic ray anisotropy measurements at these energies require the application of a filter to the data in order to remove the large uncertainty in zenith angle dependence of the cosmic ray flux; this filter also removes the axisymmetric component of the anisotropy along Earth’s rotation axis. The part of the anisotropy that comes through this filter is robustly established by several experiments. The earliest map of the large scale anisotropy, referred to as the *NFJ model*, was made by Nagashima, Fujimoto, and Jacklyn by combining data from several different experiments in the northern and southern hemispheres [4]. The excess and deficit cones were obtained by interpolating between one dimensional anisotropy measurements made in several different declination strips. Because the data used were from very different detector types (shallow underground muon telescopes vs. surface air shower array) with correspondingly large spread in energy sensitivity and very different systematic uncertainties, the result was qualitative in nature. More recently, large detectors with correspondingly large statistics and good pointing accuracy have come on line, and each one is able to make a map of the large scale anisotropy. We, as well as the Tibet air shower experiment [27], have published such maps, and both agree well with each other, as well as with that of [4].

A unique interpretation of the observed anisotropy is not possible, but it is useful to categorize the interpretations into two classes: (1) the true anisotropy is dominated by the dipole term, and (2) the higher harmonics are not negligible. If scenario (1) were true, then the distortion introduced by the analysis method projects the dipole onto the equatorial plane. Also, an excess cone and deficit cone should exist in 180° opposition to each other. The cones found in this analysis are both centered close to the equatorial plane; however, they are separated in right ascension by 130° , which is in apparent contradic-

tion to the dipole-dominant hypothesis. Quantitatively, a χ^2 fit of the data to an equatorial dipole gives a 13% chance that the observed map is consistent with a pure equatorial dipole hypothesis. Thus the data do not rule out this scenario.

Before discussing scenario (2), let us consider the implications of this scenario. Considering the complicated nature of the origins and propagation of cosmic rays, it is reasonable to assume that several different mechanisms contribute to the overall observed anisotropy; each mechanism contributes a dipole term to the map, and the observed dipole is a sum over all the dipoles projected onto the equatorial plane. One component of the dipole is due to the Compton-Getting effect. Since the nature of the other mechanisms is unknown, it is not possible to extract the Compton-Getting term. If, however, we make the extreme interpretation that the Compton-Getting effect is the dominant term, then one can extract the equatorial projection of the relative velocity between the cosmic ray rest frame and the solar system. The χ^2 fit described above gives $\tilde{D} = (7.7_{-1.5}^{+1.7}) \times 10^{-4}$ and $\alpha_0 = 32^\circ \pm 12^\circ$ with $\chi^2/\text{d.o.f.} = 577/538$ (see Eqn. 13). This corresponds to a relative velocity of 49_{-10}^{+11} km/s in the direction $32^\circ \pm 12^\circ$ right ascension. The speed is significantly smaller than the orbital speed of the solar system around the Galaxy (≈ 200 km/s), while it is comparable to the relative speed of neighboring stars around the sun. Unless there is an accidental cancellation of large dipole terms, the observed speed should be about the magnitude of the actual Compton-Getting speed. Thus one can deduce that, very likely, cosmic rays in the neighborhood of the solar system move around the galaxy with a motion similar to stars. In other words, the cosmic ray rest frame is dragged along with stars.

Let us now consider scenario (2), i.e. higher harmonic terms are not negligible. For this scenario, we focus on the particular form where two independent cones – one with an excess flux and the other with a deficit – produce the observed anisotropy. The right ascension of the cone center is not affected by the distortion, whereas the declination may or may not be significantly distorted. Specifically, if the true declination of the excess cone center is similar to that of the deficit cone, then the observed declination value should be equal to the true value (to within statistical uncertainty). On the other hand, if there is a mismatch in the declination values, then the true values are farther apart than observed – i.e. the filter causes the reconstructed cone declination values to get pushed towards each other. According to Table II, the observed declination of the excess cone center is -5° , while that of the deficit cone is $+5^\circ$; these two values are close to each other, indicating that the true values couldn't have been too far from the equator. To put this statement on a quantitative footing, the data were compared with anisotropy maps formed with different assumptions regarding the true parameter values of the excess and deficit cones. Each cone is defined by four parameters: the position of the cone center (two param-

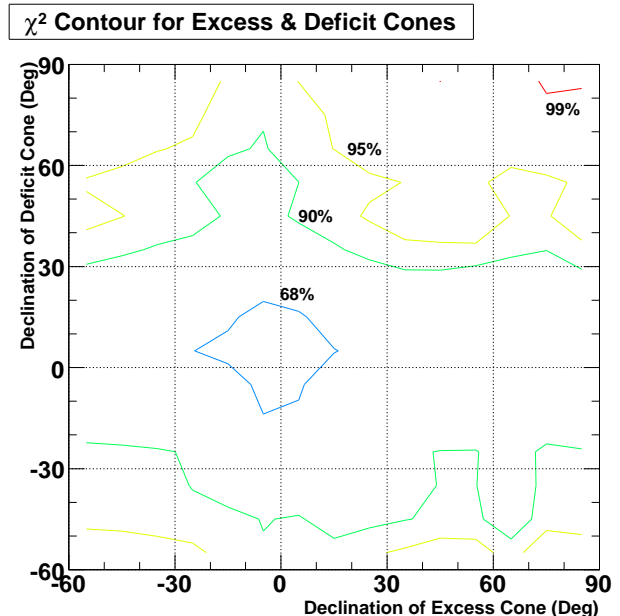


FIG. 6: A map of the marginalized χ^2 in the parameter space defined by the declination of the excess and deficit cones. At each point in the map, χ^2 was minimized with respect to the four remaining parameters.

eters), the opening angle, and the amplitude (assumed to be constant within the cone). The right ascension of each cone was fixed to the observed value since it is not distorted by the analysis filter. There are, thus, six free parameters that describe the two cones. Each set of parameter values gives rise to a value of χ^2 when compared against the data. The absolute minimum $\chi^2/\text{d.o.f.}$ of 544/534 occurs near the set of values given in Table II. A marginalized χ^2 map is shown in Fig. 6. The figure shows χ^2 as a function of declination of the excess and deficit cone center. At each point in the map, χ^2 was minimized with respect to the remaining four parameters. The contour shows the confidence level with which any pair of declination values is allowed. At 90% confidence level, the declination of the excess cone is completely unconstrained. A more stringent constraint is attainable with the deficit cone declination, but at 99% level, it also becomes almost totally unconstrained.

Let us explore the implications of the scenario where the observed cones are close to the true ones. A natural coordinate system for interpreting cosmic ray anisotropy in these energies is galactic. Figs. 4 (c) and (d) show the anisotropy map in galactic coordinates, (c) showing the fractional variation from isotropy, while (d) shows the standard deviation of this variation. One feature that clearly stands out is the large deficit seen in the Galactic northern hemisphere. This may be related to the fact that the solar system is displaced to the north of the Galactic equator by about 15 pc, a significant fraction of the half-width of the Galactic disk of about 100~200 pc. Since the cosmic ray density is almost certainly great-

est at the equator and tapering off with vertical distance away from it, the density is less to the north than to the south as viewed from the solar system. This will tend to produce a deficit flux in the Galactic north. Another observation in this regard is the fact that the deficit is less pronounced in the direction of the Orion arm. The solar system is currently located at the edge of this arm and moving towards it. It is a standard view that the cosmic ray density is elevated in the spiral arms compared to the gap regions. Thus a density gradient is likely to produce an excess flux from the Orion arm as viewed from the solar system; this excess flux may be canceling out the deficit flux from the Galactic north. We note that these observations essentially the same as those made in [28]. A final unexplained feature is the excess cone. We are unaware of any Galactic features that may cause this. The proponents of the NFJ model [4] point out that it is more-or-less aligned with the tail direction of the heliosphere; however, no plausible physical mechanism exists that could explain the size of the observed anisotropy [29].

VI. CONCLUSION

An anisotropy map of cosmic rays of nominal energy of 10 TeV was made from 1662 days of observation. The right ascension projection of this map has a first harmonic amplitude and phase of $(6.64 \pm 0.98 \text{ (stat.)} \pm 0.55 \text{ (syst.)}) \times 10^{-4}$ and $(33.2^\circ \pm 8.2^\circ \text{ (stat.)} \pm 5.1^\circ \text{ (syst.)})^\circ$, which are in good agreement with results from other experiments. The sky map indicates a region with $(0.104 \pm 0.020)\%$ excess flux in the constellation of Taurus, while a region with $(0.094 \pm 0.014)\%$ deficit flux is observed in the constellation of Virgo. The excess region is centered at $(\alpha_T, \delta_T) = (75^\circ \pm 7^\circ, -5^\circ \pm 9^\circ)$ with a half opening angle of $39^\circ \pm 7^\circ$, while the corresponding values for the deficit region are $(\alpha_V, \delta_V) = (205^\circ \pm 7^\circ, 5^\circ \pm 10^\circ)$ and half opening angle = $54^\circ \pm 7^\circ$. These regions largely coincide with those of the NFJ model, and also with those observed by the Tibet collaboration. This agreement between experiments using very different measurement techniques spanning several decades of observation and covering primary cosmic ray energies of ~ 1 to ~ 100 TeV indicates the robustness of the observed anisotropy pattern. The pattern, therefore, is a real feature of the cosmic ray flux in the neighborhood of the solar system at the current epoch. The simplest model for the observation is a pure dipole pattern, which could be produced by the Compton-Getting effect, but could also be the leading harmonic term from other more complicated mechanisms. Our observation is not described very well with a pure dipole pattern, although, at 13% confidence level, we cannot rule it out. The distorting effect of the filter applied to the data prevents us from making a unique physical interpretation of the observation. If, however, it is assumed that the distortion is not too great, the deficit region coincides with a large portion of the Galac-

tic northern hemisphere. This may be related to the fact that the solar system is displaced by about 15 pc to the north of the Galactic plane. Also, the deficit appears to be canceled out in the direction of the Orion Arm, which may be an indication of enhanced levels of cosmic ray density there. The excess region does not seem to match any features that could provide a mechanism for its existence, though it has been noted [4] that it points in the direction of the tail end of the heliosphere.

Acknowledgments

We gratefully acknowledge the cooperation of the Kamioka Mining and Smelting Company. The Super-Kamiokande experiment has been built and operated from funding by the Japanese Ministry of Education, Culture, Sports, Science, and Technology, the United States Department of Energy, and the U.S. National Science Foundation. Some of us have been supported by funds from the Korean Research Foundation (BK21) and Korea Science and Engineering Foundation, the Polish Committee for Scientific Research (grant 1P03B08227), Japan Society for the Promotion of Science, and Research Corporation's Cottrell College Science Award.

APPENDIX A: SUBTRACTING THE ANISOTROPY DUE TO ATMOSPHERIC EFFECTS

The observed sidereal anisotropy is due to two effects: extra-terrestrial (i.e. Compton-Getting, Galactic, and heliospheric effects) and atmospheric (due to residual effects of seasonal and solar diurnal variations in the atmospheric temperature). Since we are interested only in the extra-terrestrial anisotropy, it is desirable to subtract the atmospheric contribution. We discuss in this Appendix technical details on this subtraction. The method is due to Farley and Storey [2], which is applied to the zenith-type plot. In the second section this result is generalized to the two dimensional anisotropy map. Finally, the results of the first two sections are used to subtract the atmospheric contribution from the track-type one dimensional plot.

1. Subtraction for the Zenith-Type Plot

The zenith-type plot is equivalent to the relative variation in the muon rate as a function of local sidereal time. In Farley and Storey's formulation, the rate variation is parameterized generally as follows:

$$R(t) = 1 + \underbrace{[A + 2B \cos 2\pi(t - \phi_2)]}_{\text{SEASONAL MODULATION}} \underbrace{\cos 2\pi(Nt - \phi_1)}_{\text{SOLAR VARIATION}} + \underbrace{C \cos 2\pi\{(N+1)t - \phi_3\}}_{\text{TRUE SIDEREAL VARIATION}}, \quad (\text{A1})$$

where t is measured in years, $N \approx 365.24$ cycles/year is

$$R(t) = 1 + \underbrace{A \cos 2\pi(Nt - \phi_1)}_{\text{SOLAR}} + \underbrace{B' \cos 2\pi\{(N+1)t - (\phi_1 + \phi_2)\}}_{\text{SPURIOUS SIDEREAL}} + \underbrace{C \cos 2\pi\{(N+1)t - \phi_3\}}_{\text{TRUE SIDEREAL}} + \underbrace{B \cos 2\pi\{(N-1)t - (\phi_1 - \phi_2)\}}_{\text{PSEUDO-SIDEREAL}} \quad (\text{A2})$$

The first time dependent term in Eqn. A2 is the relative rate variation with a periodicity of one solar day, the second and third terms are rate variations with a periodicity of one sidereal day, and the final term is the rate variation with a periodicity of one pseudo-sidereal day, which is longer than the solar diurnal day by about 0.27% (Figs. 7 (a)-(c)). Written in this form, it is seen that there are two sources of sidereal variation, the “spurious” one due to the atmosphere and the “true” one due to extraterrestrial effects.

Each time dependent term in Eqn. A2 can be represented by phasors. In Cartesian coordinates, they are given as follows:

$$\begin{aligned} \vec{A} &= (A \cos \phi_1, A \sin \phi_1) \\ \vec{B}' &= (B' \cos(\phi_1 + \phi_2), B' \sin(\phi_1 + \phi_2)) \\ \vec{C} &= (C \cos \phi_3, C \sin \phi_3) \\ \vec{B} &= (B \cos(\phi_1 - \phi_2), B \sin(\phi_1 - \phi_2)) \end{aligned}$$

The phasor \vec{A} is non-zero due to residual effects of the solar diurnal and seasonal variation in the atmospheric temperature, while $\vec{D} = \vec{C} + \vec{B}'$ is non-zero primarily due to extra-terrestrial effects (represented by \vec{C}), although, in general, a non-zero contribution is also made by atmospheric effects (represented by \vec{B}'). No real effect is directly responsible for a non-zero value of \vec{B} , but, as described above, interplay between seasonal and solar diurnal variation in the atmospheric temperature can indirectly give rise to a non-zero magnitude.

In terms of phasors, one sees that the process of measuring the true sidereal variation involves measuring the phasor \vec{B}' and subtracting it from \vec{D} . The phasor \vec{D} is obtained from Fig. 7 (a), while \vec{B}' is obtained from \vec{B} and \vec{A} , which are, in turn, obtained from Figs. 7 (b) and

the solar diurnal frequency, and ϕ_i , $i = 1, 2, 3$ are phase angles. The parameters A , B , and C are the magnitude of the relative rate variation for different periodicities (discussed below). The solar diurnal variation is assumed to be seasonally modulated (first line, Eqn. A1). The second line represents the true sidereal variation (i.e. of extra-terrestrial origin). A re-arrangement of the first line above gives the following:

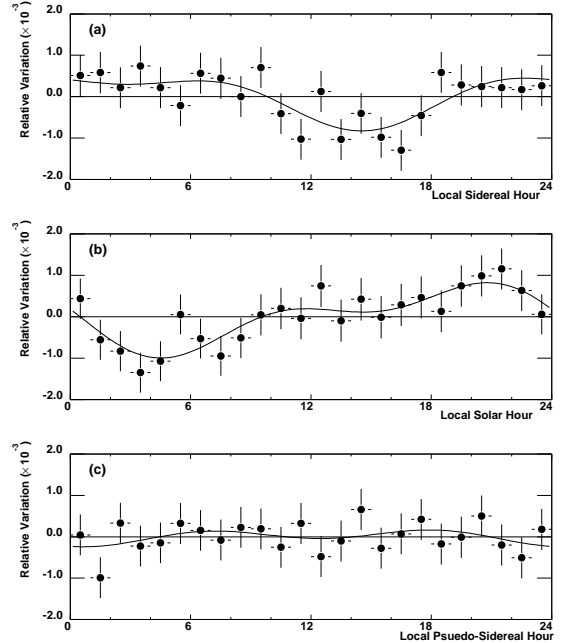


FIG. 7: (a) Relative muon rate as a function of local sidereal time (i.e. zenith-type map), in hours right ascension. (b) Relative muon rate as a function of local solar hour. (c) Relative muon rate as a function of hours, pseudo-sidereal time. The curve in each frame is the best fit of the first two harmonic functions to the data.

(c). Specifically, \vec{B}' is obtained by reflecting \vec{B} about the axis defined by \vec{A} (see Fig. 8 (a)).

\vec{B}' and \vec{C} can be obtained approximately by using the most likely value of \vec{A} , \vec{B} , and \vec{D} . These are given as $\vec{B}'(\text{CALC})$ and $\vec{C}(\text{CALC})$ in Table III. A statistically rig-

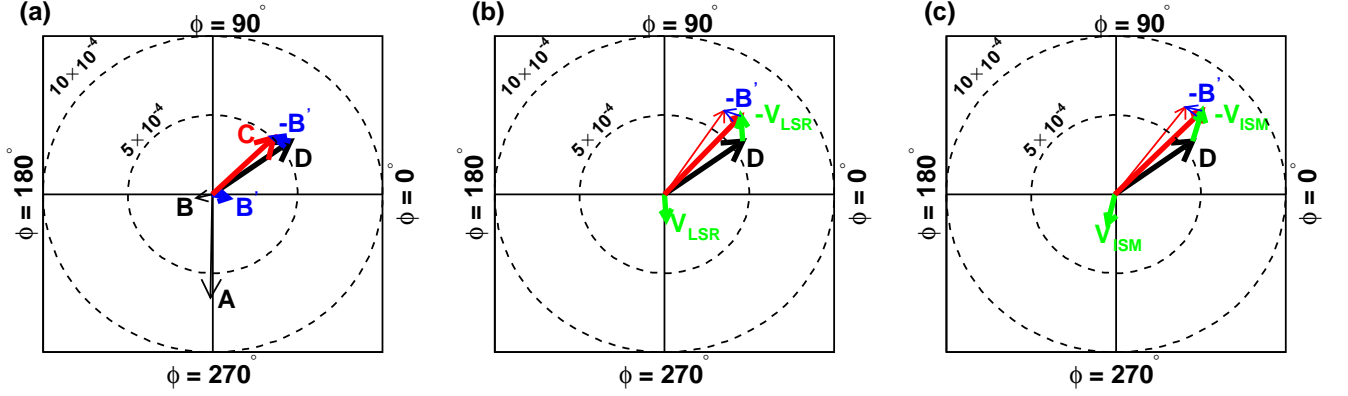


FIG. 8: Phasor diagrams showing the result of subtracting the atmospheric and Compton-Getting effects. The length of an arrow represents the amplitude of the first harmonic component, while the angle measured counter clockwise from $\phi = 0^\circ$ is the phase at maximum. (a) Atmospheric effect, (b) Compton-Getting effect assuming cosmic ray rest frame moving with the local standard of rest, and (c) same as (b), but moving with the local interstellar medium. In each plot, the vector \vec{D} indicates the uncorrected amplitude and phase, while the vector $-\vec{B}'$, $-\vec{V}_{\text{LSR}}$, and $-\vec{V}_{\text{ISM}}$ are corrections for the atmospheric and Compton-Getting effects. The vectors \vec{A} , \vec{B} , and \vec{C} are defined in the text. (b) and (c) also show the result of subtracting both effects.

PHASOR	AMP ($\times 10^{-4}$)	PHASE (HR)
\vec{A}	6.63 ± 0.98	18.0 ± 0.6
\vec{B}	1.01 ± 0.98	13.1 ± 3.7
\vec{D}	5.65 ± 0.98	2.3 ± 0.7
\vec{B}' (CALC)	1.01	22.9
\vec{C} (CALC)	5.09	2.9
\vec{B}' (STAT)	0.98 ± 0.71	23.2 ± 5.2
\vec{C} (STAT)	5.31 ± 1.19	2.7 ± 0.9

TABLE III: Summary of phasor parameters. \vec{A} , \vec{B} , and \vec{D} are from data (N.B. the amplitude and phase of \vec{D} are slightly different from those shown in Table I because of difference in binning); \vec{B}' (CALC) and \vec{C} (CALC) are calculated directly from the first three, while \vec{B}' (STAT) and \vec{C} (STAT) are obtained by the statistical subtraction technique described in the text.

orous determination of \vec{C} and associated uncertainties require the use of a statistical subtraction technique in which the phasors \vec{A} , \vec{B} , and \vec{D} are generated randomly according to their respective χ^2 probability from the first harmonic fits in Fig. 7. For each generated triplet of phasors, there corresponds a unique value of \vec{C} , and an ensemble of generated \vec{C} gives a distribution of $|\vec{C}|$ and ϕ_C . The mean and RMS of a Gaussian fit to each are taken as the most likely value and uncertainty of the true sidereal anisotropy; these are given as \vec{C} (STAT) in Table III.

2. Subtraction for the Two Dimensional Map

We describe in this section the method used to subtract the anisotropy of atmospheric origin from the two dimensional anisotropy map. Letting M denote a two

dimensional map, the true (i.e. corrected) map M_{TRUE} is given by:

$$M_{\text{TRUE}} = M_{\text{OBS}} - M_{\text{ATM}}, \quad (\text{A3})$$

where M_{OBS} is the observed map, and M_{ATM} is the map of anisotropy of atmospheric origin. M_{ATM} is calculated by assuming that: (1) the incident cosmic ray flux is isotropic (the observed anisotropy introduces only a second order correction, so it can be ignored); (2) the atmospheric effect causes the overall cosmic ray rate to vary with amplitude and phase given by the phasor \vec{B}' , i.e. amplitude = 0.98×10^{-4} and phase = 348° right ascension.

The map M_{ATM} is obtained by convoluting the relative rate variation $R(\tau_s) = 1 + |B'| \cos(\omega_s \tau_s - \phi_{B'})$ with the isotropic event rate $I(\delta, h)$, where τ_s is sidereal time, ω_s is the sidereal angular frequency, δ is the declination, $h = \alpha - \tau_s$ is the hour angle, and α is the right ascension. Note that I has units of $\text{day}^{-1} \text{m}^{-2} \text{sr}^{-1}$; it is related to Fig. 1 by a coordinate transformation. The convolution is as follows:

$$M_{\text{ATM}}(\delta, \alpha) = \int d\tau_s I(\delta, \alpha - \omega_s \tau_s) R(\tau_s) \quad (\text{A4})$$

The map M_{ATM} (from which the δ dependence is factored out) is shown in Fig. 9 (a). The excess and deficit cone parameters for M_{TRUE} are shown in Table IV. The direction and cone size of the deficit region are unchanged by this correction, whereas those of the excess region change noticeably.

REGION TYPE	NAME	CONE SOURCE	(α, δ)	SIZE	DEVIATION	χ
EXCESS	TAURUS	NO CORRECTION	$(65^\circ, 5^\circ)$	27°	0.140%	5.26σ
		ATM	$(75^\circ, -5^\circ)$	39°	0.104%	5.31σ
		CG, LSR	$(85^\circ, -35^\circ)$	65°	0.0964%	6.46σ
		CG, ISM	$(55^\circ, 5^\circ)$	60°	0.0884%	6.95σ
		ATM + CG, LSR	$(85^\circ, -35^\circ)$	65°	0.0991%	6.65σ
	ATM + CG, ISM	$(55^\circ, 5^\circ)$	60°	0.0877%	6.90σ	
	TAIL-IN	NFJ MODEL	$(90^\circ, -24^\circ)$	68°	—	—
DEFICIT	VIRGO	NO CORRECTION	$(205^\circ, 5^\circ)$	54°	-0.0988%	-7.27σ
		ATM	$(205^\circ, 5^\circ)$	54°	-0.0940%	-6.91σ
		CG, LSR	$(215^\circ, 5^\circ)$	55°	-0.107%	-7.95σ
		CG, ISM	$(215^\circ, 5^\circ)$	55°	-0.115%	-8.57σ
		ATM + CG, LSR	$(215^\circ, 5^\circ)$	55°	-0.103%	-7.66σ
	ATM + CG, ISM	$(215^\circ, 5^\circ)$	55°	-0.111%	-8.28σ	
	GALACTIC	NFJ MODEL	$(180^\circ, 20^\circ)$	57°	—	—

TABLE IV: Cone parameters of excess and deficit regions. The column ‘‘Cone Source’’ refers to the data set or model from which the cones are derived. ‘‘No Correction’’ refers to the anisotropy without any subtraction, while the other rows refer to that after subtracting various effects. ‘‘ATM’’ is the atmospheric effect, ‘‘CG, LSR (ISM)’’ is the equatorially projected Compton-Getting effect with the cosmic ray rest frame assumed to be the same as the local standard of rest (local interstellar matter). ‘‘ATM + CG, LSR (ISM)’’ is that from which both effects are subtracted. Columns 4 and 5 show the center and half opening angle of the cones. Column 6 shows the deviation from the isotropic event rate in the contained regions, and column 7 (χ) shows the statistical significance of the deviation.

3. Subtraction for the Track-Type Map

The track-type one dimensional map corrected for atmospheric effects can be obtained by simply projecting $M_{\text{TRUE}}(\delta, \alpha)$ onto the right ascension axis. However, this does not provide an estimate of the uncertainty introduced by the atmospheric subtraction. In order to obtain this, we first generate an ensemble of phasors \vec{D} , \vec{A} , and \vec{B} , as described in Sec. A 1. For each triplet, a two dimensional map M_{TRUE} is made, as described in Sec A 2. This map is then projected onto right ascension axis to obtain the one dimensional map. The first two harmonic functions (Eqn. 18) are then fit to each map thus obtained. We thus obtain an ensemble of fit values A_1 and ϕ_1 (the second harmonic is unchanged in the ensemble because the atmospheric effect was assumed to have only first harmonic variation). The result of this procedure is given in Table I in the row labeled ‘‘TRACK/CORR.’’. The first error is statistical (from fitting harmonic functions to the data), and the second error is from the dispersion in the fit values obtained from the ensemble method described above.

APPENDIX B: CORRELATION BETWEEN MUON RATE AND ATMOSPHERIC TEMPERATURE

The effect of the atmosphere on the cosmic ray detection rate in underground muon detectors is, in general, correlated with the pressure at the detector altitude and with the atmospheric temperature profile above the detector. The pressure dependence becomes unimportant compared to temperature dependence for muon threshold

energy greater than about 100 GeV [30].

In this limit, the relative change in the muon rate with atmospheric temperature is given by the following expression:

$$\frac{\delta I}{I} \approx \int_0^{x_0} \alpha(x, \bar{E}_0, x_0) \delta T(x) dx \quad (\text{B1})$$

The quantity α is the partial temperature coefficient, $\delta T(x)$ is the deviation of the temperature from the mean at atmospheric depth x , \bar{E}_0 is the threshold muon energy, and x_0 is the atmospheric depth at the detector altitude. The mechanism for the temperature dependence of the rate is as follows. As the temperature rises, the atmospheric density decreases, and the probability that a meson in a cosmic ray shower is destroyed by interaction with air nuclei decreases. The increased meson mean free path implies that mesons have increased chance to decay and produce muons. The cosmic ray muon rate, therefore, is positively correlated with atmospheric temperature. The partial temperature coefficient can be calculated numerically using inputs such as a model atmosphere, primary cosmic ray flux, particle production cross section, particle decay constants, etc.[30], while $\delta T(x)$ can be obtained at discrete atmospheric levels from meteorological measurements. For SK-I, the change in rate due to this effect should be $\approx \pm 1\%$, which is more than an order of magnitude larger than the magnitude of the sidereal anisotropy.

Figure 10 (a) shows the relative variation in the muon rate for each month and year of SK-I. The solid curve shows the predicted variation based on Eqn. B1 [31]. The temperature measurements were obtained from the Wajima Observatory (37.38° N, 136.90° E, 116 km from the

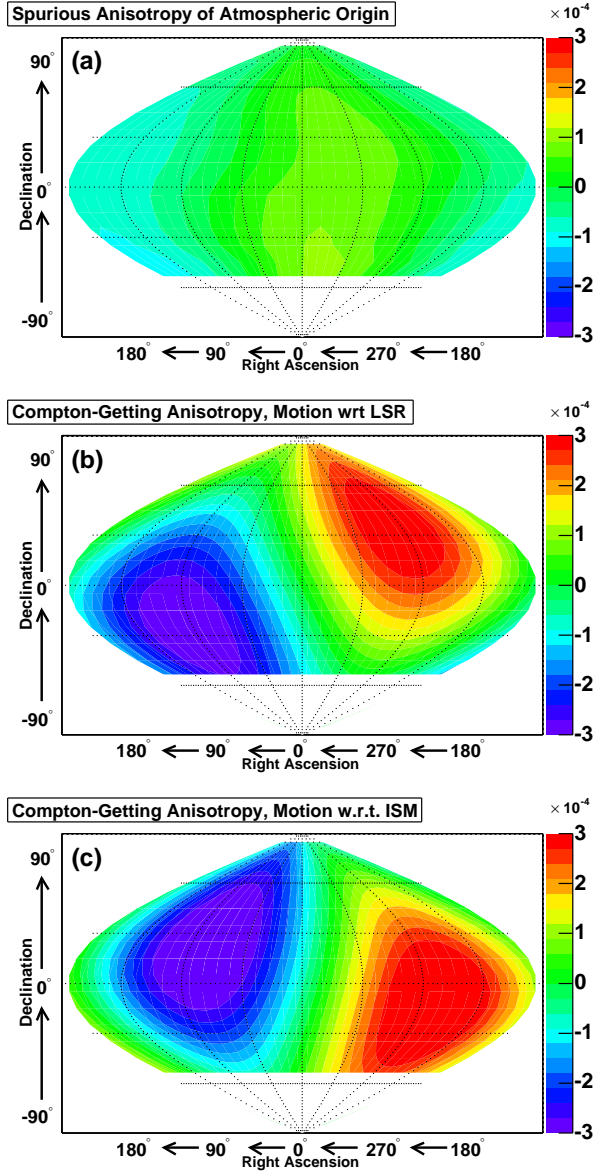


FIG. 9: Anisotropy introduced by: (a) the atmospheric effect; (b) the Compton-Getting effect assuming that the bulk cosmic ray motion is the same as the local standard of rest; (c) same as (b), but the motion is assumed to be the same as that of the neutral interstellar matter. The contour values indicate fractional deviation from isotropy. The white region below declination of -53.58° is always below the horizon. Note that the filter applied to the data projects the anisotropy shown in (b) and (c) onto the equatorial plane.

SK-I detector) [32]. Radio sonde was used to measure the temperature of 25 layers of the atmosphere between 1000 mb and 5 mb. These measurements were made twice a day. The agreement between the data and prediction is good, though not perfect. The disagreement is due to inaccuracies in the temperature measurements at altitudes above 40 mb. At SK-I energies, the partial temperature coefficient increases all the way to very shallow atmo-

spheric depths, so inaccurate temperature measurements at altitude above 40 mb (i.e. pressure < 40 mb) introduce significant inaccuracies in the predicted rate.

A better standard for checking the SK-I rate variation is by means of a simultaneous independent measurement from a nearby underground muon detector. The Matushiro detector (36.53 N, 138.01 E, 79 km from SK-I) is perfectly suited for this requirement [33]. With an overburden of 220 m.w.e., its muon energy threshold is about 100 GeV. This lower energy threshold implies that the rate variation at Matushiro is similar to that of SK-I, but has smaller amplitude (see Fig. 10 (b)).

One measure of this difference is the month to month variation in $\Delta I/I$ at the two sites. According to calculation [31], the magnitude of this change at SK-I should be 2.03 times larger than that at Matushiro. A correlation plot of the changes at the two sites is shown in Fig. 11. The regression coefficient $\beta = 2.03 \pm 0.05$ is in agreement with the predicted value.

When the data are binned in solar diurnal hours, the 1% level monthly variations almost cancel out, leaving a residual variation at the level of several parts per ten thousand. This variation, when modulated seasonally, produces side band components with frequency 365.24 ± 1 cycles per year. The frequency of 366.24 cycles per year is the inverse of one sidereal day, and the existence of this component implies that the observed sidereal variation in the cosmic ray rate is partly due to atmospheric temperature variations. This contribution to the observed sidereal anisotropy can be estimated using the method of Farley and Storey [2]. A detailed discussion of the atmospheric contribution to the sidereal anisotropy is given in Appendix A.

APPENDIX C: SUBTRACTING THE COMPTON-GETTING ANISOTROPY

The Compton-Getting effect refers to the enhancement of the cosmic ray flux in the observer's direction of motion relative to the reference frame in which the bulk motion of the cosmic ray plasma is at rest. If the observer's velocity relative to the cosmic ray bulk motion is \vec{v} and the direction of observation is in the direction of the unit vector \hat{u} , the relative enhancement in the intensity is given by:

$$\frac{\Delta I}{I} = (2 + \gamma) \frac{v}{c} \cos \chi, \quad (C1)$$

where $v = |\vec{v}|$, c is the speed of light in vacuum, and $\cos \chi = \vec{v} \cdot \hat{u}/v$ is the cosine of the opening angle between the observer's motion and the direction of observation. The cosmic ray rest frame is not known, although the observed smallness of the anisotropy implies that its motion relative to the sun must be small (v/c must be on the order of 10^{-4} , or $v \lesssim 30$ km/s, barring an accidental large cancellation of the Compton-Getting

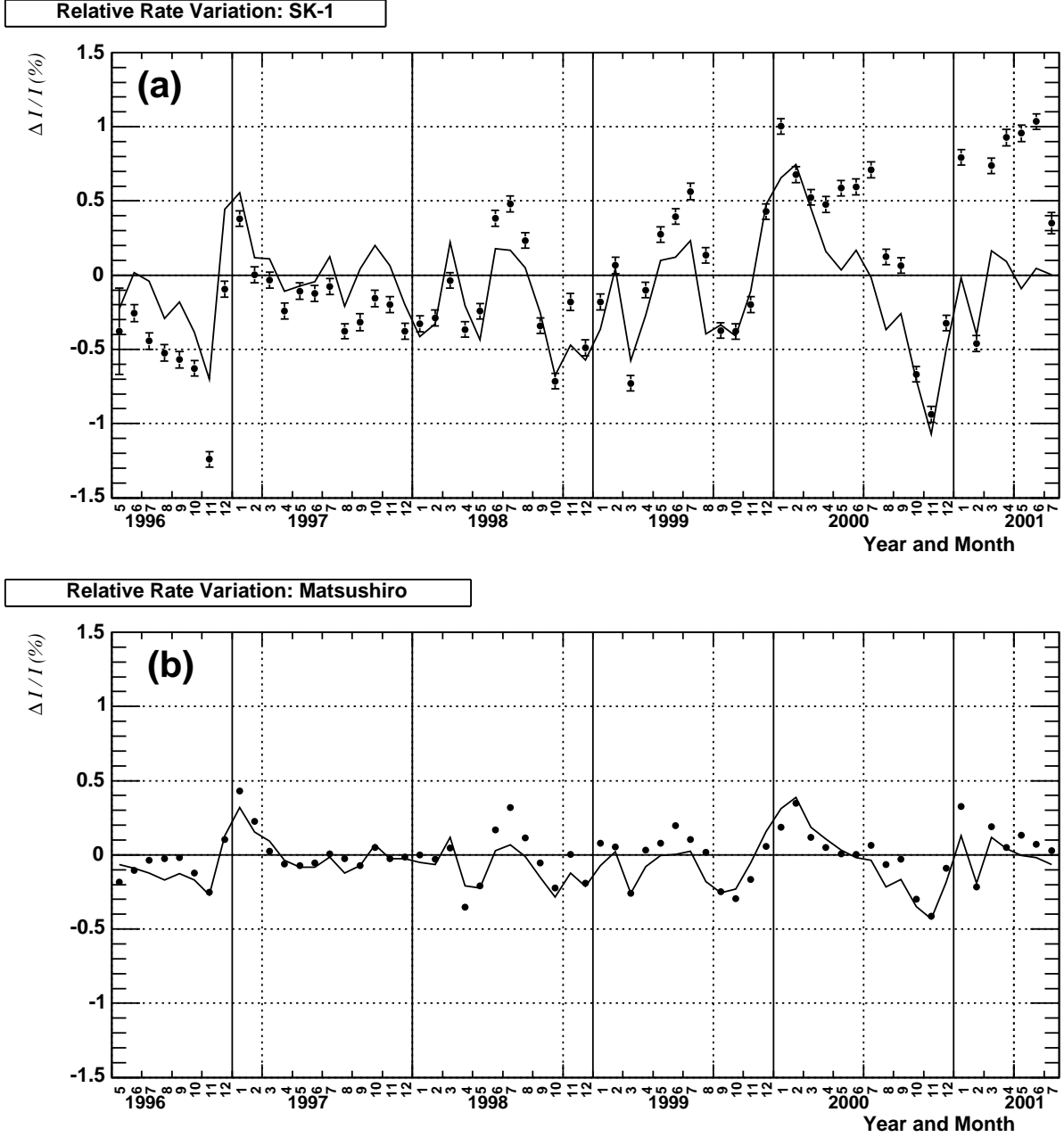


FIG. 10: (a) Variation in the muon rate relative to the mean for each month of SK-I. (b) The variation seen at Matsushiro during the same period. The solid curve in each frame is the predicted rate variation based on equation B1.

anisotropy by that due to other effects). Two assumptions are often invoked in the literature: the cosmic ray rest frame is at rest with respect to (1) the local standard of rest, or (2) the local interstellar medium. The first motion has speed $v_{\text{LSR}} \approx 20$ km/s in the direction $(\alpha_{\text{LSR}}, \delta_{\text{LSR}}) \approx (270^\circ, 29.2^\circ)$, while the second motion has speed $v_{\text{ISM}} \approx 22$ km/s in the direction $(\alpha_{\text{ISM}}, \delta_{\text{ISM}}) \approx (252^\circ, -17^\circ)$. The values were chosen to be consistent with [4]; see references therein for citations for these values. The dipole anisotropy due to the Compton-Getting effect is shown in Figs. 9 (b) and (c). As mentioned in

Section III, the filter applied to the data projects the dipole onto the equatorial plane, so the center of the observed dipole has no declination component, and the effective velocity is the equatorial projection of the velocity, which is $v_{\text{LSR}} \cos \delta_{\text{LSR}} = 17$ km/s for motion with respect to the local standard of rest, and $v_{\text{ISM}} \cos \delta_{\text{ISM}} = 21$ km/s for motion with respect to the interstellar medium. The cone parameters before and after subtracting the equatorial projection of the Compton-Getting anisotropy from the observed anisotropy are summarized in Table IV.

We also examined the effect of the Compton-Getting

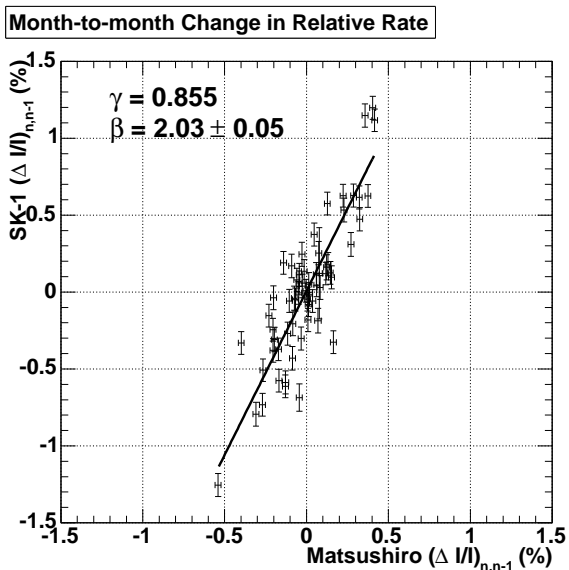


FIG. 11: The correlation between $(\Delta I/I)_{n,n-1}$, SK-1 vs. Matsushiro. $\Delta I/I$ is the relative rate variation of a given month; the notation $(\Delta I/I)_{n,n-1}$ indicates the difference of this quantity between month n and $n-1$. $\gamma = 0.855$ is the linear correlation coefficient between the two data (60 degrees of freedom), while $\beta = 2.03 \pm 0.05$ is the best fit slope.

anisotropy on the one dimensional anisotropy. Since the track- and zenith-type plots are very similar, we focus here on just the zenith-type plot. Starting with the two dimensional Compton-Getting anisotropy map (Figs. 9 (b) and (c)) and folding in the effect of the overburden (Fig. 1), the one dimensional anisotropy due to the Compton-Getting effect alone is described well by a first harmonic function with amplitude and phase (1.66×10^{-4} , 274°) for cosmic ray bulk motion with the local standard of rest, and (2.00×10^{-4} , 256°) for bulk motion with the interstellar matter. These two anisotropies are indicated by the phasors \vec{V}_{LSR} and \vec{V}_{ISM} in Fig. 8 (b) and (c). The amplitude and phase of the observed anisotropy without any subtraction are indicated in the figure as \vec{D} . The contribution of the Compton-Getting anisotropy is removed by subtracting $\vec{V}_{\text{LSR,ISM}}$ from \vec{D} : the result is also shown in the figure. The anisotropy is enhanced, and the direction of anisotropy rotates toward 90° . The effect of atmospheric subtraction is also shown. The amplitude and phase of the anisotropy before and after subtraction are summarized in Table V. Also shown

in the table are the anisotropies after subtracting both effects.

APPENDIX D: THE CLUSTERING ALGORITHM

The clustering algorithm is applied to a histogram $N_{i,j}$, where $N_{i,j}$ is the exposure-corrected number of events in bin (i,j) , $i =$ right ascension bin index, $j =$ declination

SUBTRACTION	AMPLITUDE	PHASE (DEG)
NONE	5.7×10^{-4}	35°
CG, LSR	6.7×10^{-4}	48°
CG, ISM	7.3×10^{-4}	45°
ATMOSPHERIC	5.3×10^{-4}	40°
CG, LSR + ATMOSPHERIC	6.5×10^{-4}	52°
CG, ISM + ATMOSPHERIC	7.0×10^{-4}	50°

TABLE V: Amplitude and phase of the zenith-type one dimensional anisotropy before and after subtractions. CG, LSR refers to the Compton-Getting effect assuming cosmic ray rest frame moving with the local standard of rest, while CG, ISM refers to the case where the cosmic ray is assumed to move with the local interstellar matter.

bin index. For each (i,j) , the quantity χ is calculated over a variable sized cone centered on (i,j) , where:

$$\chi = \frac{N_{\text{obs}} - N_{\text{exp}}}{\sqrt{N_{\text{exp}}}} \quad (\text{D1})$$

N_{obs} is the observed number of events in the cone, and N_{exp} is the expected number in the absence of anisotropy. The cone size (half opening angle) that extremizes χ is sought; the excess/deficit is assumed significant if $|\chi| > 4$. If the center of one cone falls within another cone, the cone with small $|\chi|$ is rejected.

The statistical error of the reconstructed cone parameters was estimated using an ensemble experiment technique in which an input sky map with anisotropy cones with parameters given in Table II was used to generate a large number of output maps with random statistical fluctuations. The clustering algorithm was applied to each generated map, and the distribution of the reconstructed cone parameters was examined. The RMS of these distributions were taken as the statistical error.

-
- [1] A. H. Compton and I. A. Getting, Phys. Rev. **47**, 817 (1935).
 [2] F. J. M. Farley and J. R. Storey, Proc. Phys. Soc. A **67**, 996 (1954).
 [3] K. Nagashima et al., Nuovo Cimento C **12**, 695 (1989).
 [4] K. Nagashima, K. Fujimoto, and R. M. Jacklyn, J. Geo-

phys. Res. No. A8 **103**, 17429 (1998).

- [5] Such a map was made using data from the IMB experiment and was reported in Gary McGrath's Ph. D. thesis [34], but the statistical significance was marginal and it was not published. The anisotropy reported there is qualitatively similar to our observation.

- [6] S. Fukuda et al., Nucl. Instr. Meth. A **501**, 418 (2003).
- [7] H. Ishino, Ph.D. thesis, University of Tokyo (1999).
- [8] Y. Kajiyama, Master's thesis, Osaka University (2001).
- [9] K. Murakami et al., Nuovo Cimento C **2**, 635 (1979).
- [10] K. Munakata et al., Phys. Rev. D **56**, 23 (1997).
- [11] M. Ambrosio et al., Phys. Rev. D **67**, 042002 (2003).
- [12] D. B. Swinson and K. Nagashima, Planet. Space Sci. **33**, 1069 (1985).
- [13] K. Nagashima et al., Planet. Space Sci. **33**, 395 (1985).
- [14] H. Ueno et al., Proc. of the 21st International Cosmic Ray Conference **6**, 361 (1990).
- [15] T. Thambyahpillai, Proc. of the 18th International Cosmic Ray Conference **3**, 383 (1983).
- [16] K. Munakata et al., Proc. of the 24th International Cosmic Ray Conference **4**, 639 (1995).
- [17] S. Mori et al., Proc. of the 24th International Cosmic Ray Conference **4**, 648 (1995).
- [18] M. Bercovitch and S. P. Agrawal, Proc. of the 17th International Cosmic Ray Conference **10**, 246 (1981).
- [19] K. B. Fenton et al., Proc. of the 24th International Cosmic Ray Conference **4**, 635 (1995).
- [20] Y. W. Lee and L. K. Ng, Proc. of the 20th International Cosmic Ray Conference **2**, 18 (1987).
- [21] D. J. Cutler and D. E. Groom, Astrophys. J. **376**, 322 (1991).
- [22] Y. M. Andreyev et al., Proc. of the 20th International Cosmic Ray Conference **2**, 22 (1987).
- [23] K. Munakata et al., Proc. of the 26th International Cosmic Ray Conference **7**, 293 (1999).
- [24] V. V. Alexeenko et al., Proc. of the 17th International Cosmic Ray Conference **2**, 146 (1981).
- [25] M. Aglietta et al., Proc. of the 24th International Cosmic Ray Conference **2**, 800 (1995).
- [26] T. Gombosi et al., Proc. of the 14th International Cosmic Ray Conference **2**, 586 (1975).
- [27] M. Amenomori et al., Science **314**, 439 (2006).
- [28] T. I. Gombosi et al., Nature **225**, 687 (1975).
- [29] K. Munakata et al., Proc. of the 26th International Cosmic Ray Conference **7**, 263 (1999).
- [30] S. Sagisaka, Nuovo Cimento C **9**, 809 (1986).
- [31] Calculation performed by K. Munakata, Shinshu University, 2004.
- [32] *Aerological Data of Japan*, ed. Japan Meteorological Agency (monthly issue).
- [33] Data from the Matsushiro Observatory was provided to us by K. Munakata, Shinshu University, 2004.
- [34] G. G. McGrath, Ph.D. thesis, University of Hawaii, Manoa (1993).
- [35] The systematic uncertainty on the true magnitude, 10%, is significantly smaller than the magnitude of the spurious anisotropy, 18%, because the statistical correction technique involves addition of phasors, which are two-dimensional vectors. Significant cancellation occurs when the vectors are added statistically.